

Geophysical Research Letters[®]



RESEARCH LETTER

10.1029/2023GL104088

Ice Shelf Water Structure Beneath the Larsen C Ice Shelf in Antarctica

Ji Sung Na¹ , Peter E. D. Davis² , Byeong-Hoon Kim¹ , Emilia Kyung Jin¹ , and Won Sang Lee¹ 

¹Division of Glacial Environment Research, Korea Polar Research Institute, Incheon, Republic of Korea, ²Polar Oceans Group, British Antarctic Survey, London, UK

Key Points:

- Direction and magnitude of ocean currents beneath an Larsen C ice shelf affect the ice shelf water thickness and properties
- Northward meltwater advection causes 0.052°C difference of thermal drivings with different melt rates far from and near the grounding line
- Ocean heat intrusion to ice shelf base is induced by Ekman dynamics and thermohaline interleaving by tilted isopycnals

Supporting Information:

Supporting Information may be found in the online version of this article.

Correspondence to:

E. K. Jin,
jin@kopri.re.kr

Citation:

Na, J. S., Davis, P. E. D., Kim, B.-H., Jin, E. K., & Lee, W. S. (2023). Ice shelf water structure beneath the Larsen C Ice Shelf in Antarctica. *Geophysical Research Letters*, 50, e2023GL104088. <https://doi.org/10.1029/2023GL104088>

Received 19 APR 2023

Accepted 11 AUG 2023

Author Contributions:

Conceptualization: Ji Sung Na, Byeong-Hoon Kim, Emilia Kyung Jin, Won Sang Lee

Data curation: Won Sang Lee

Formal analysis: Ji Sung Na, Peter E. D. Davis, Byeong-Hoon Kim, Emilia Kyung Jin, Won Sang Lee

Funding acquisition: Won Sang Lee

Investigation: Ji Sung Na, Peter E. D. Davis, Emilia Kyung Jin, Won Sang Lee

Methodology: Ji Sung Na, Peter E. D. Davis, Byeong-Hoon Kim

Project Administration: Won Sang Lee

Resources: Emilia Kyung Jin

Abstract Understanding ice shelf water (ISW) structure is crucial for studying the basal melting of ice shelves. In this study, we performed large-eddy simulation experiments to assess ISW structure and basal melt patterns under different current velocity scenarios observed in the Larsen C ice shelf, Antarctica. The LES results revealed that the thickness of ISW is primarily determined by the meridional velocity (perpendicular to the grounding line), while the zonal velocity influences the potential temperature and salinity of ISW. We found that a key parameter determining the basal melt rate was northward meltwater advection which originates from variances in meltwater generation. This advection, in turn, leads to the tilted isopycnals and the potential for thermohaline interleaving in a diffusive convection regime. The different slopes of isopycnals induce distinct heat fluxes, resulting in different basal melt rates far from and near the grounding line (~0.44 and 1.59 m yr⁻¹, respectively).

Plain Language Summary The loss of ice mass from the Antarctic ice sheet is accelerating, posing a threat to human lives through global sea level rise. Understanding ice shelf water (ISW), which refers to seawater below freezing temperature, is crucial as it directly or indirectly influences basal ice melting. However, direct observations are extremely challenging, leaving this understanding unclear. To tackle this issue, we utilized a numerical model to gain insight into the fundamental characteristics of ISW. We demonstrated that the direction and magnitude of ocean currents beneath the ice shelf play a significant role in determining the thickness and properties of ISW. Moreover, the key factor in basal melting was the northward movement of meltwater from intense ice melting regions near the grounding line. This movement determined the spatial distribution of ocean temperature and salinity. The horizontal gradient of ocean temperature and salinity induces mixing and horizontal intrusion. Interestingly, these mixing and intrusion phenomena occur in opposite directions, resulting in a wiggling pattern in the velocity profile. The main findings of our study will contribute to the formulation of a parameterization for basal melting, which can be incorporated into large-scale ocean models or ice sheet dynamics models.

1. Introduction

Basal melting near the grounding line of Antarctic ice shelves is one of the major factors controlling the ice shelf stability, ice sheet loss, and sea level rise (Alley et al., 2016; Pritchard et al., 2012; Rignot et al., 2013). Ice mass loss from the Antarctic ice sheet—a major contributor to global sea level rise—is modulated by the reduced buttressing effect of its peripheral ice shelves, and basal melting-induced retreat of the grounding line (Dinniman et al., 2016). Over the past decade, the Antarctic ice loss has accelerated with a dramatic increase in West Antarctic ice mass loss and a decrease in East Antarctic ice mass gain (Paolo et al., 2015; Rignot et al., 2019).

Basal melting occurs when ocean heat penetrates the stratification layer of the ice shelf water (ISW) near the basal ice surface (Begeman et al., 2018; Milillo et al., 2019). This is because the meltwater interferes heat entrainment to ice base (negative feedback for the basal melting), enhancing the stratification between the fresh, lighter meltwater and the salty ocean (Hewitt, 2020). However, this stratification can be weakened by external forces (e.g., strong tide, high thermal driving, and melt-driven circulation) that can be different for each Antarctic ice shelf. In warm-water cavity ice shelves with a steeply sloping ice base (e.g., Thwaites and Pine Island), the presence of Circumpolar Deep Water causes strong basal melting (e.g., 50–100 m yr⁻¹) because of the highly turbulent melt-driven circulation (Holland et al., 2020; Nakayama et al., 2019, 2021; Stanton et al., 2013). In contrast, in cold-water cavity ice shelves (e.g., Ross, Larsen C, and Filchner–Ronne), moderate melt rates (1–2 m yr⁻¹) occur

© 2023. The Authors.

This is an open access article under the terms of the [Creative Commons Attribution-NonCommercial-NoDerivs License](https://creativecommons.org/licenses/by/4.0/), which permits use and distribution in any medium, provided the original work is properly cited, the use is non-commercial and no modifications or adaptations are made.

Software: Byeong-Hoon Kim
Supervision: Emilia Kyung Jin, Won Sang Lee
Validation: Ji Sung Na, Emilia Kyung Jin
Writing – original draft: Ji Sung Na, Emilia Kyung Jin
Writing – review & editing: Ji Sung Na, Peter E. D. Davis, Byeong-Hoon Kim, Emilia Kyung Jin, Won Sang Lee

owing to an energetic flow environment caused by strong tidal currents and their interactions with the seabed despite a weak thermal driving (Arzeno et al., 2014; Davis & Nicholls, 2019; Mueller et al., 2012).

In previous numerical modeling efforts for diagnostic studies (Mueller et al., 2012; Nakayama et al., 2019) and future predictions (Timmermann & Hellmer, 2013) of the Antarctic ocean water mass and sub-ice shelf circulation, ice shelf basal melting is parameterized using the three equation model (Hellmer & Olbers, 1989; Holland & Jenkins, 1999; Jenkins, 1991) with turbulent transfer coefficients and far-field values of temperature and salinity (Diniman et al., 2016; Jenkins, 2016; McPhee, 2008; Vreugdenhil & Taylor, 2019). However, because these coefficients and far-field values vary dramatically in different turbulent environments, they are difficult to specify. Model predictions adopting incorrect transfer coefficients and far-field values can be in huge disagreement with actual observations. These uncertainties stand out near the grounding line because of its strongly variable nature (P. R. Holland, 2008). Therefore, we need to carefully choose the values of three equation model, based on in situ observation or high-resolution turbulence modeling results.

To resolve these uncertainties, various observational studies (hot-water drilling (HWD) observations, autonomous underwater vehicle, etc.) have been conducted for observing the ice–ocean boundary near the grounding line (Davis & Nicholls, 2019; Jenkins et al., 2010). However, the detailed structure of turbulent mixing within the ice–ocean boundary layer could not be sufficiently understood because of the coarse spatial resolution. If we can employ a suitable numerical model based on observations to quantify the turbulent mixing and heat entrainment within the ice–ocean boundary, various parameterizations can be developed to reduce the uncertainty in the future predictions of basal melting and ice mass loss.

The Larsen C Ice Shelf (LCIS) is a cold-water cavity ice shelf and several studies have been carried out to investigate the properties of ocean currents and tide characteristics within the ice shelf cavity (Davis & Nicholls, 2019; Mueller et al., 2012; Nicholls et al., 2012). Given small thermal driving in the LCIS, it becomes more important to delve into the effects of turbulent heat entrainment, which is highly related to the ocean current velocity, on basal melting (Davis & Nicholls, 2019; Vreugdenhil & Taylor, 2019). However, the spatial distribution of basal melting and its relationship with turbulent heat entrainment are challenging to observe.

In this study, we conduct large eddy simulation (LES) experiments to assess the relationship between ocean currents and ISW structures and related physics beneath the LCIS. The experiment set up, including the domain configuration, basal roughness, transfer coefficients and far-field values, was determined based on the in situ HWD observations beneath LCIS (Davis & Nicholls, 2019).

2. Data and Methods

2.1. Numerical Model

To simulate the oceanic boundary layer flow with basal melting beneath an ice shelf, the Parallelized Large-Eddy Simulation Model (PALM) was employed (Maronga et al., 2015; Na et al., 2022; Raasch & Schröter, 2001). The detailed numerical schemes (e.g., time integration, flow advection, pressure solver, and turbulence closure) were set equal to those of a previous LES study on the ice–ocean boundary layer (Na et al., 2022).

To consider the thermal and saline changes caused by melting at the ice–ocean boundary, we formulated the potential temperature and salinity fluxes q_{θ^*} and q_{S^*} based on the Monin–Obukhov similarity with ice–ocean interface values (θ_b and S_b), which are determined by the liquidus condition (Ramudu et al., 2018).

$$q_{\theta^*} = \tau_{\theta} [\theta(z_1) - \theta_b] u_* \quad (1)$$

$$q_{S^*} = \tau_S [S(z_1) - S_b] u_* \quad (2)$$

$$\theta_b = \lambda_1 S_b + \lambda_2 + \lambda_3 P, \quad (3)$$

$$c_w \rho_w \tau_{\theta} u_* (\theta_f - \theta_b) = \rho_i L_i m, \quad (4)$$

$$\rho_w \tau_S u_* (S_f - S_b) = \rho_i S_b m, \quad (5)$$

where τ_{θ} and τ_S are the non-dimensional transfer coefficients of heat and salt, respectively, and u_* is friction velocity, which is calculated at each time step. In this case, various τ_{θ} and τ_S were set, based on thermal Stanton

number, $C_d^{1/2} \Gamma_\theta = 0.0011$ and different drag coefficients at each velocity observed in Davis and Nicholls (2019) (e.g., $\tau_\theta C_d = 0.01227, 0.00804$ at 3 cm s^{-1} , $\tau_\theta C_d = 0.01637, 0.00452$ at 6 cm s^{-1} , and $\tau_\theta C_d = 0.02009, 0.003$ at 10 cm s^{-1}). The coefficients ratio, $\tau_\theta \tau_s$ was set to 35. z_j is the uppermost grid, P is the hydrostatic pressure, $\lambda_1 = -0.0573^\circ\text{C}$, $\lambda_2 = 0.0832^\circ\text{C}$, and $\lambda_3 = -0.000753^\circ\text{C dbar}^{-1}$ (Ramudu et al., 2018). m is the basal melting rate and subscripts w and i represent water and ice, respectively. The specific heat capacity of water is $c_w = 2,974 \text{ J kg}^{-1}\text{C}^{-1}$, and the latent heat of fusion is $L_i = 3.35 \times 10^5 \text{ J kg}^{-1}$.

To obtain ice–ocean interface values by solving equations for the effect of pressure on interface values (Equation 3) and liquidus condition (Equations 4 and 5), we need far-field values (θ_f and S_f). In this study, we used the averaged values (-2.01°C , 34.55 psu) within the ISW layer as the far-field values, obtained by the in situ HWD observation. Using the thermal driving between these ice–ocean interface values and the simulated ocean temperature ($\theta(z_i) - \theta_b$), the basal fluxes of temperature and salinity (Equations 1 and 2, respectively) were applied at the first grid cell nearest the ice base.

2.2. Experimental Description

We constructed our simulation environment based on in situ HWD observations. Davis and Nicholls (2019) reported that the ice draft and water column thickness at the location of the borehole were 301 and 192 m, respectively. The ice draft at the grounding line closest to the borehole location ($\sim 12 \text{ km}$) was estimated to be approximately 253 m (Morlighem et al., 2020), which yielded a difference of 48 m between the ice shelf base at the borehole and the grounding line. We assumed the ice shelf base and seabed topography to be linear. The basal roughness length, z_{or} , was 0.5 mm, which was comparable to 0.44 mm proposed in the HWD observation study. The simulation domain was set from 3 km away to 15.288 km away from the grounding line with linear slopes of ice shelf and seabed.

The total scale of our domain was $12,288 \text{ m} \times 6,144 \text{ m} \times 294 \text{ m}$ in the x , y , and z directions, respectively. A 12 m horizontal and 1.5 m vertical grid was used to compose the simulation domain ($1,024 \times 512 \times 196$ grid cells). The scale of the vertical grid was comparable to the mixing length obtained from the HWD observations. These grid confinements yielded appropriate level of turbulent kinetic energy ($1.0 \times 10^{-3} \text{ m}^2 \text{ s}^{-2}$) near the ice shelf base, which was similar to that from the HWD. We employed the Monin-Obukhov similarity fluxes since our grid resolution cannot resolve the near-wall physics. It enables our LES model to resolve the three-dimensional structures of the ISW with turbulent mixing and heat entrainment. The vertical dimension of 294 m represents the depth range from 265 to 559 m (Figure 1a).

Here, u (meridional) and v (zonal) velocities represent the velocities in the perpendicular and parallel directions to the grounding line, respectively. For the velocity, the inlet boundary condition (left side) was set to the Dirichlet boundary condition for a geostrophic current of different velocities, while those for the potential temperature and salinity were set to the Dirichlet boundary conditions with constant values of -1.96°C and 34.575 psu , respectively. The outlet boundary condition (right side) was set to radiation boundary condition that imposes little effect on waves in the domain interior (Na et al., 2022). Initial conditions were set to values of inlet boundary condition, assuming that the situation without the ISW. The periodic boundary condition (outflow at $y = 0 \text{ m}$ is applied to inflow at $y = 6,144 \text{ m}$) was applied to lateral boundaries, while a no-slip condition was imposed at the seabed and the ice base. In summary, these LES experiments were constrained by initial condition, inlet boundary conditions, and boundary layer fluxes at the ice shelf and seabed.

In this study, we conducted 11 LES experiments, including a control case ($v = 6 \text{ cm s}^{-1}$, $u = 1.5 \text{ cm s}^{-1}$), an averaged velocity case ($v = 8 \text{ cm s}^{-1}$, $u = 1.5 \text{ cm s}^{-1}$), no melting case (no melting effect), different v cases ($v = 3, 4, 5, 7, 9$ and 10 cm s^{-1} with $u = 1.5 \text{ cm s}^{-1}$) and different u cases ($v = 6 \text{ cm s}^{-1}$ with $u = 0.5$ and 1 cm s^{-1}), based on the in situ results in the HWD observation (Davis & Nicholls, 2019).

A random generator for small velocity perturbations at depths of 270–554 m was applied to quickly spin up the small-scale turbulence (Li & Van Roekel, 2021). The adopted time step was applied under the condition: Courant number = 0.9. The total simulation time was 89 hr, and friction velocity (u_*) converged at 0.2643 cm s^{-1} after 73.5 hr, which corresponds to $14 t^*$ (large-eddy turnover time, $t^* = 5.25 \text{ hr}$: ISW depth/friction velocity). The friction velocity in each different velocity case also converged after 73.5 hr. In this study, we used the time-averaged results from 73.5 to 89 hr ($\sim 3 t^*$ after the flow converged) to observe the quasi-steady features. Detailed information on the target region and physical dimension of the simulation domain with the geometry length scale are summarized in Figure 1a.

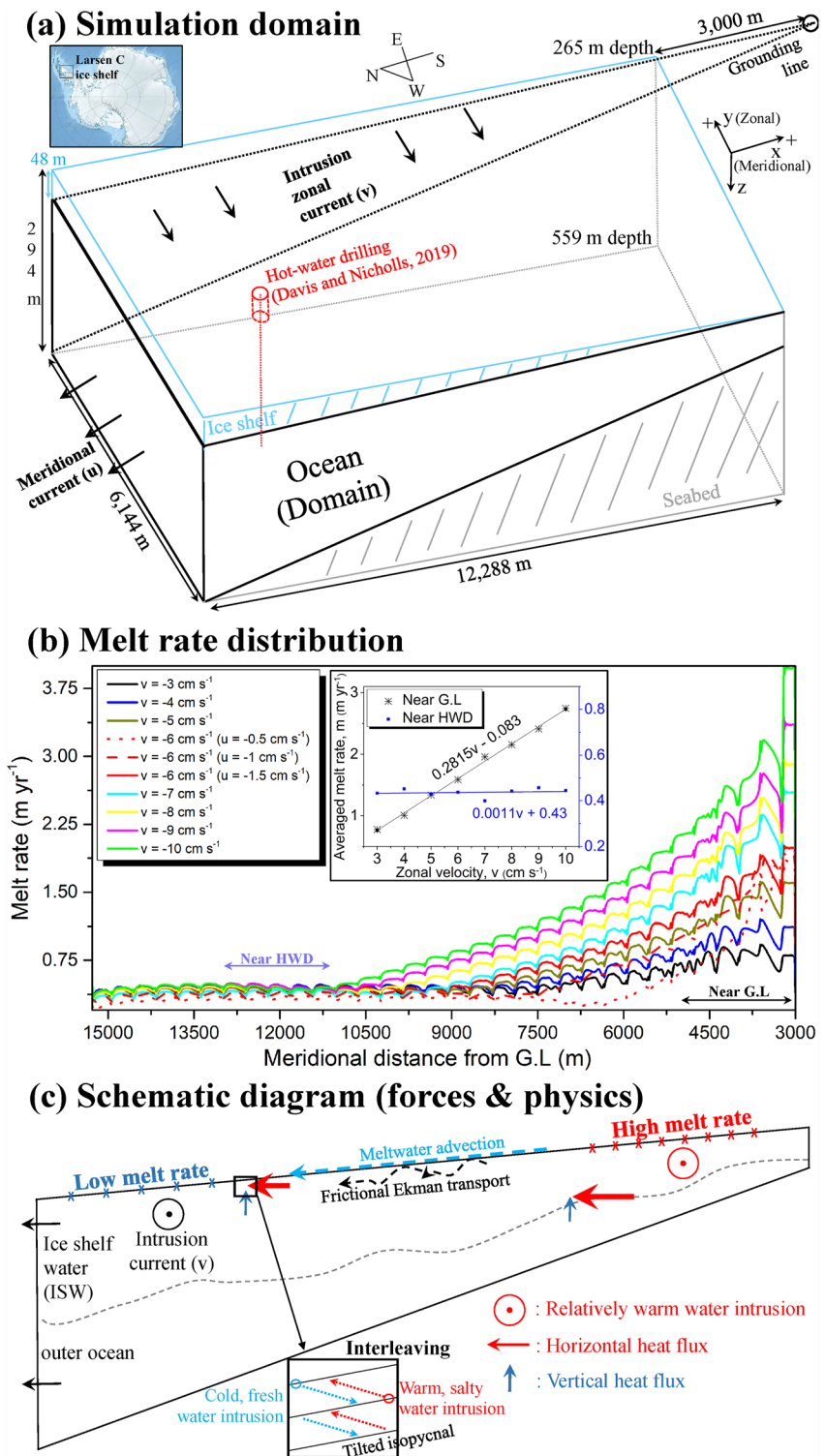


Figure 1. (a) Location of LCIS in Antarctica and domain configuration of the ice shelf, ocean, and seabed with descriptions of the boundary conditions (b) Meridional distribution of basal melt rate (m yr⁻¹) for 10 different velocity cases. The inset plot represents the relationship between the zonal velocity and the melt rates. (c) Schematic diagram of the various force balance, which are the main physics related to basal melting and ISW structure.

3. Results

3.1. The Impacts of Currents on Melt Rate and ISW

The distribution and magnitude of the basal melt rate was different in all 10 different velocity cases (Figure 1b). All of melt rate near the grounding line was higher than that far from (near the HWD) the grounding line. The effect of the zonal velocity on the basal melt rate far from and near the grounding line (x , distance from the grounding line = 11,000–13,000 m and 3,000–5,000 m) was different. With increasing zonal velocity, the melt rate near the grounding line increased rapidly, but those far from the grounding line increased slightly. This was because of the difference of thermal drivings far from and near the grounding line (Figure S1a in Supporting Information S1). As the zonal velocity increased, friction velocity increased linearly (Figure S1b in Supporting Information S1). However, thermal driving near the grounding line in all cases was similar, while thermal driving far from the grounding line in the 10 cm s⁻¹ case was 3.1 times lower than that in the 3 cm s⁻¹ case. In the control case, the difference of thermal driving far from and near the grounding line was 0.052°C. This heterogeneous distribution of thermal driving subsequently led to variances in both the melt rates and quantity of meltwater in meridional direction. It induced the coherent northward meltwater advection in conjunction with the frictional Ekman transport and the meridional component of geostrophic current. In the control case, a basal melt rate of 0.44 m yr⁻¹ was observed near the HWD. This melt rate was 37% smaller than the value observed by an upper-looking sonar (0.7 m yr⁻¹, Davis & Nicholls, 2019). This difference is likely due to underestimated vertical mixing by the lack of tides and the assumption of a smooth, linearly varying ice base in this study (MacAyeal, 1984).

To examine how LES experiments resolve ISW characteristics, we compared the vertical profiles of potential temperature and salinity in the LES results with the HWD observation results. In control case, the LES results were similar to those of the HWD observation, in terms of magnitude near the ice shelf and the ISW thickness (Figures 2a and 2b). This implies that our LES model accurately reproduced the frictional Ekman transport (frictionally generated current that flows to the right of the geostrophic current) and vertical advection of temperature and salinity within the ISW layer and properly parameterized the in situ basal melting effect. The zonal and meridional velocities had different impacts on the ISW characteristics; the zonal velocity magnitude controlled the potential temperature and salinity near the ice shelf base. However, the magnitude of meridional velocity set the ISW thickness (Figures 2a and 2b) which includes Ekman layer and thermohaline mixing layer. This is because the magnitude of meridional velocity affects the horizontal gradient of temperature and salinity, which determine the depth of thermohaline mixing layer. In Figures 2c and 2d and Figure S2 in Supporting Information S1, only 21 m Ekman layer (\sim theoretical Ekman depth, $u_* f = 0.002643 \text{ m s}^{-1} / 1.349 \times 10^{-4} \text{ s}^{-1} = 19.6 \text{ m}$) was observed in the case with no melting effect, whereas 21 m Ekman layer and 50 m thermohaline mixing layer were observed in the control case. Interestingly, vertical layering of velocity fluctuations was observed clearly within the thick ISW in the cases of high speed ($v \geq 6 \text{ cm s}^{-1}$ and $u = 1.5 \text{ cm s}^{-1}$). These velocity fluctuations were caused by thermohaline interleaving intrusion which can develop in the diffusive convection regime. Detailed evolution of the vertical layering of velocity and ISW creation can be seen in Movies S1 and S2.

3.2. Turbulent Heat Entrainment Within the ISW

In the x - z contour (y = domain center) of potential temperature, meltwater fraction, Turner angle, and density ratio ($R_\rho = \beta \Delta S / \alpha \Delta \theta$) which represents the relative contributions of temperature and salinity for the density gradient (Figure 3), we examined the ISW characteristics and double-diffusive type for thermohaline interleaving (Kimura et al., 2015; Ruddick, 1983). Potential temperature right below the ice shelf far from and near the grounding line was -2.058 and -1.987°C , respectively. The slope of the isopycnals was different in regions far from and near the grounding line. Isopycnals near the grounding line were tilted up toward the ice shelf, allowing warm water to be transported toward the ice shelf base more readily. The isopycnal spacing was narrower for higher zonal velocities, showing that stronger frictional Ekman transport caused vortex squeezing (deformed isopycnals by low pressure at vortex center) far from the grounding line (Figure S2a and Figure S3 in Supporting Information S1). In this study, ISW is defined as seawater with a meltwater fraction exceeding 0.2‰ (Figure 3b), which is determined from potential temperature and salinity (Jenkins, 1999). A relatively high meltwater fraction ($\sim 1\%$) was observed far from the grounding line, confirming the presence of northward meltwater advection. The 27.785–27.805 isopycnals, which are indicative of glacial meltwater, were located right beneath the ice shelf (Figure 3b'). We conclude that northward meltwater advection along these isopycnals of glacial meltwater is the main cause of tilted isopycnals and heterogeneous distribution of basal melting.

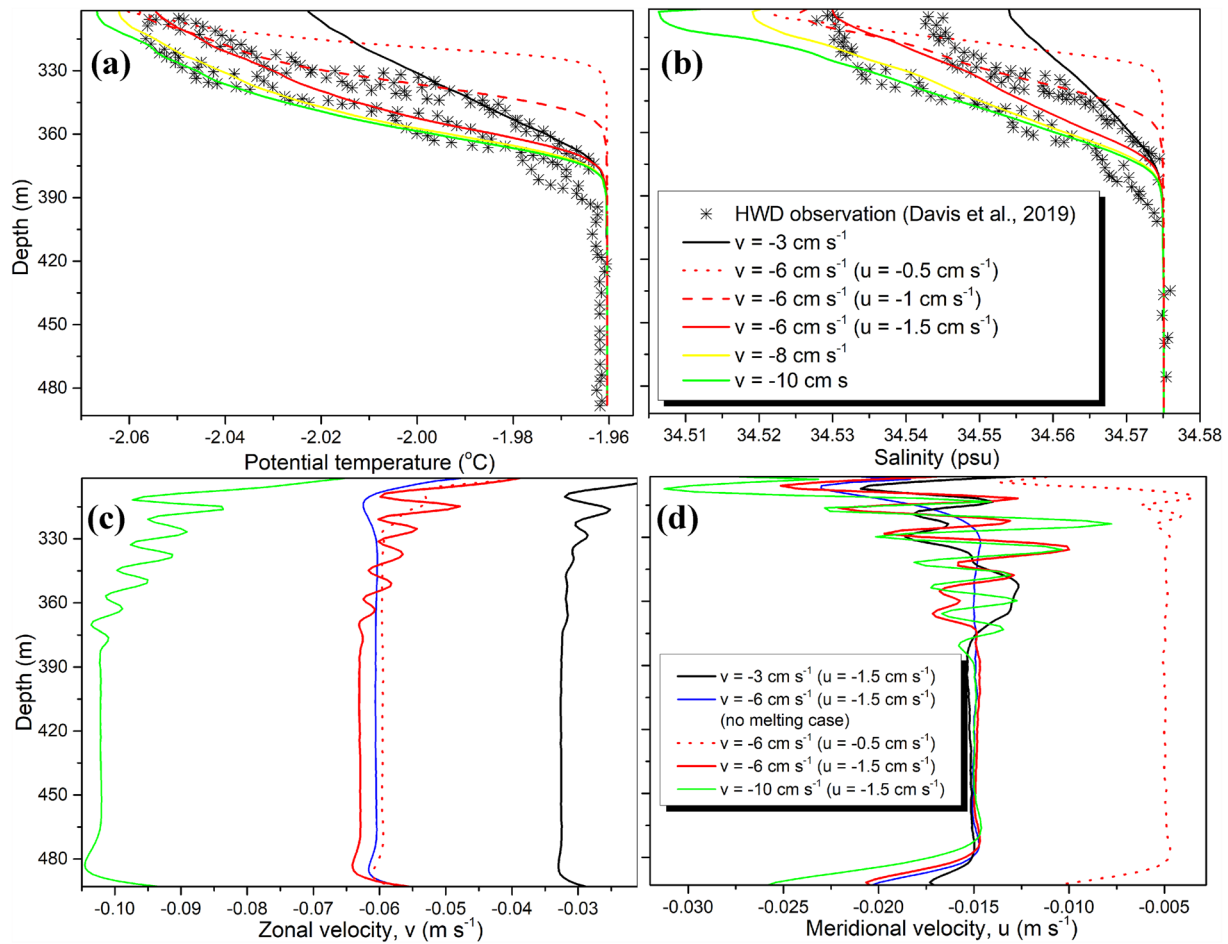


Figure 2. (a, b) Vertical profiles of potential temperature (°C) and salinity (psu) in six different velocity cases at $x = 12,000$ m and the HWD observation results. (c, d) Vertical profiles of the zonal and meridional velocities in six different velocity cases and the no melting effect case at $x = 12,000$ m.

To examine the double-diffusive convection type, we plot the Turner angle and density ratio. Within the ISW layer, diffusive convection ($-90^\circ < Tu < -45^\circ$, $R_\rho > 1$) was dominant in the region far from and near the grounding line. Diffusive convection regime (cool, fresh water overlying warm, salty water) beneath the LCIS was confirmed in HWD observation results (Figure S4 in Supporting Information S1). The high density ratio means that the destabilizing temperature profile can drive small-scale mixing (interleaving) even though the density profile is stable. This mixing was initiated by thermohaline-shear instability identified by the positive value of the maximum unstable growth rate within ISW layer (Figure S5 in Supporting Information S1). This instability grew through the release of potential energy stored in the horizontal gradients of two distinct baroclinic components (temperature and salinity).

To reveal the detailed ISW structures and evaluate the heat entrainment from the outer ocean to the ice shelf base, we illustrate the x - z contours of both horizontal and vertical heat fluxes, along with vertical profiles of the heat fluxes and stabilizing buoyancy flux in the control case in Figure 4. The magnitude of the horizontal heat flux was approximately 7–10 times larger than the vertical heat flux, indicating that along-isopycnal heat flux dominated over cross-isopycnal heat flux. The vertical structure of horizontal heat flux near the grounding line was asymmetric (Figure 4d), while that far from the grounding line was quasi symmetric (Figure 4c). Additionally, the horizontal heat flux near the grounding line was 3–4 times higher than that far from the grounding line (Figures 4a–4d). This implies that thermohaline interleaving by steep isopycnals near the grounding line was stronger than that far from the grounding line. Moreover, the vertical heat flux near the grounding line was approximately 3 times larger than that far from the grounding line. The latter was attributed to the Ekman layer and small scale interleaving intrusions at the local peak of the stabilizing buoyancy flux between 21 and 71 m in

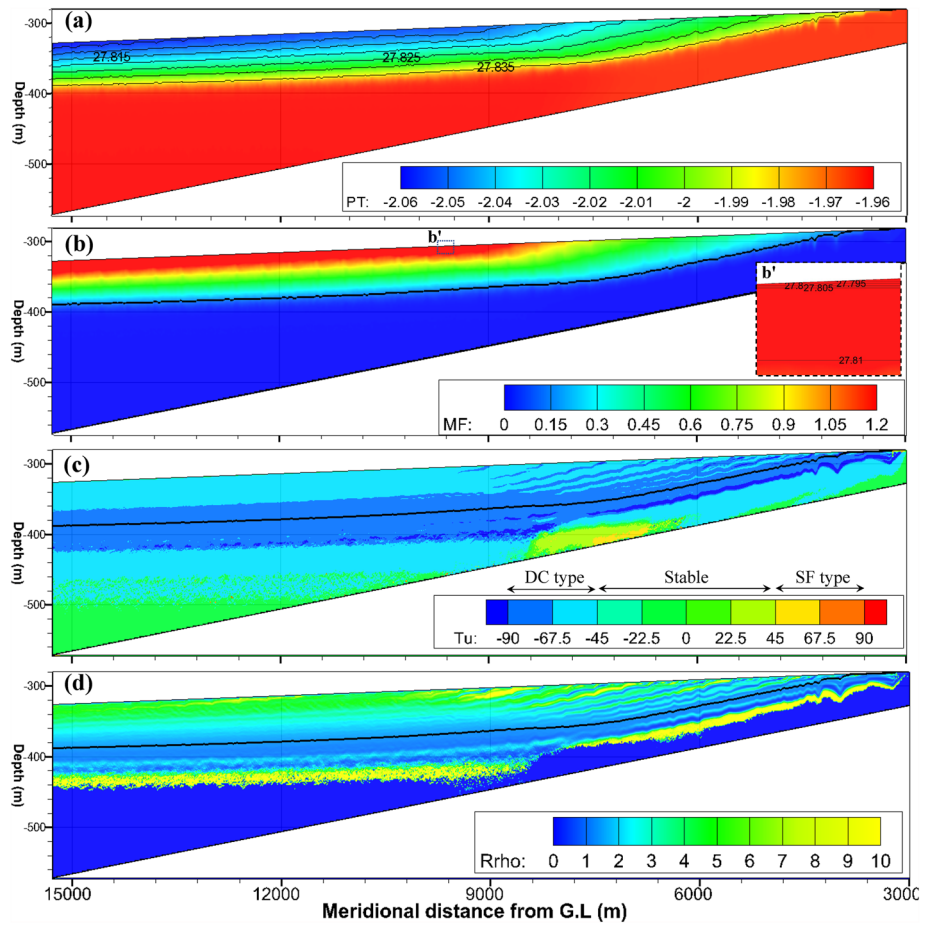


Figure 3. x - z contour (y = domain center) of (a) potential temperature with potential density lines (0.005 intervals from 27.835 kg m^{-3}). (b) meltwater fraction (%) in the control case. Meltwater fraction was obtained from two tracers (potential temperature and salinity) (Jenkins, 1999). (c) Turner angle. (d) Density ratio, R_ρ .

depth, whereas the former was caused by Ekman layer and large scale interleaving intrusion (Figures 4g and 4h). While mean vertical heat flux ($\rho c_s d\theta/dz$) was observable within the Ekman layer, the majority of vertical heat transport was dominated by the eddy vertical heat flux ($\rho c_s w'\theta'$) (Figures 4e and 4f).

4. Conclusions and Discussions

As shown in Figure 1c, meltwater behavior and ISW structure near the grounding line were controlled by frictional Ekman transport and thermohaline interleaving. In this study, we conducted a range of experiments to examine the relationship between the current velocity and ISW structure using LES.

Through comprehensive analysis of ISW layer, we demonstrate the presence of thermohaline interleavings within the ISW. However, the effect of thermohaline interleavings may be less in the reality because strong turbulence by tidal currents is dominant beneath LCIS (Rosevear et al., 2022). Because it is hard to observe this phenomenon through only in situ temperature and salinity profiles, vertical profiles of velocity along with turbulence instrument clusters will be needed to fully understand these processes and its structure.

Because these numerical experiments were focused on the oceanic and geometric conditions beneath LCIS (Kenyon peninsula), the main findings in this study are limited to the LCIS region. Therefore, the oceanographic and geometric conditions should be examined, if main findings are used to interpret ISW structures beneath other cold-water cavity ice shelves. The current understanding of the ISW structure can be broadened through additional sensitivity studies of other parameters such as slopes of the seabed, ice shelf and tidal amplitude in future studies, as well as effects of zonal and meridional velocities in this study.

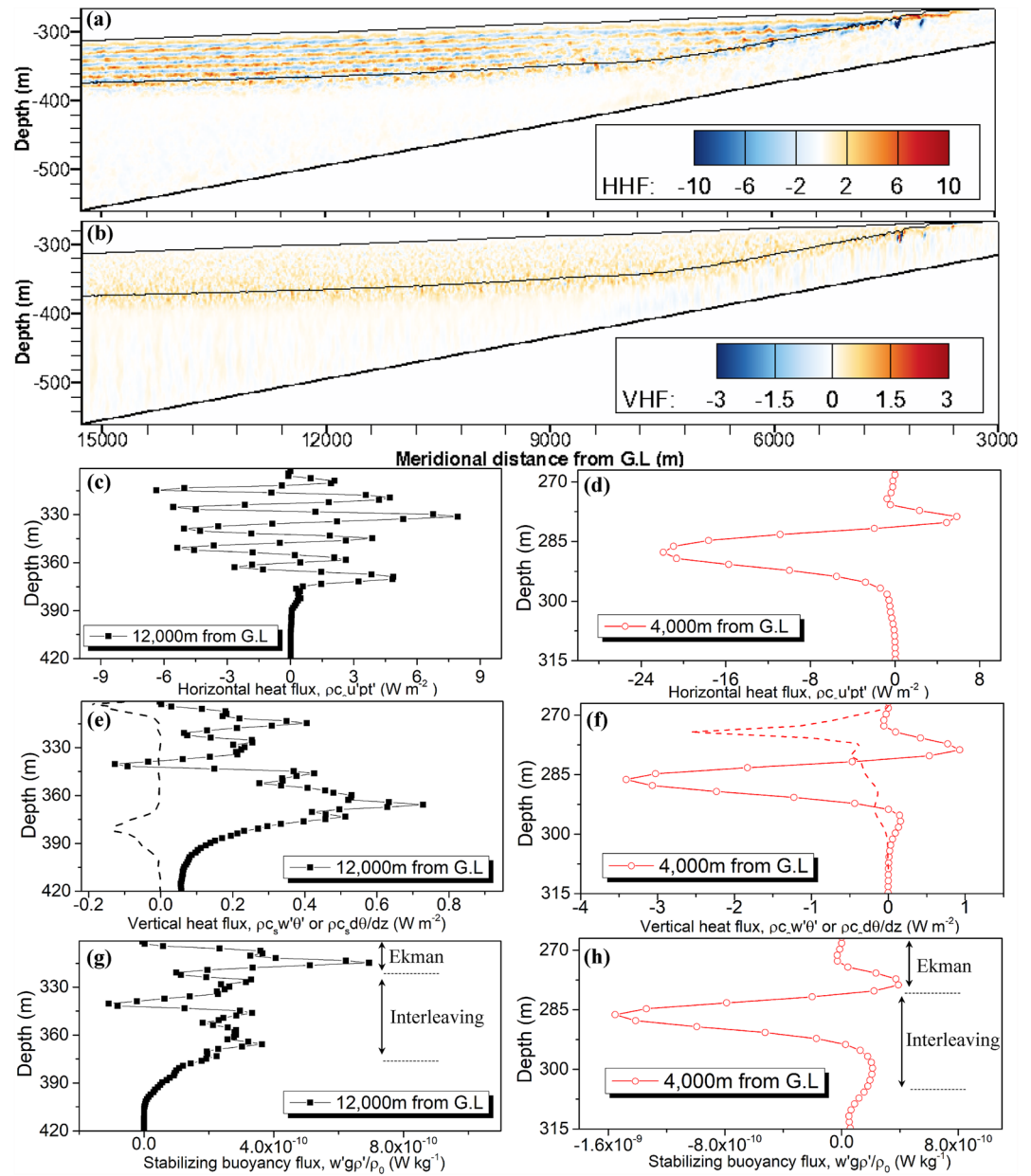


Figure 4. (a, b) x - z contours of horizontal heat flux (HHF, W m^{-2}) and vertical heat fluxes (VHF, W m^{-2}) in the control case; the black lines represent the potential density. (c, d) Vertical profiles of the HHF. (e, f) Vertical profiles of the VHF. Solid line with square represents eddy heat flux and dashed line represents mean heat flux. (g, h) Vertical profiles of the stabilizing buoyancy flux (W kg^{-1}), where ρ_0 ($1,028 \text{ kg m}^{-3}$) is the reference density of seawater, c_s ($4.02 \times 10^3 \text{ J kg}^{-1} \text{ K}^{-1}$) is the specific heat capacity of seawater, and the apostrophe indicate fluctuations in the variables (Sharqawy et al., 2010). The left column represents the location $x = 12,000 \text{ m}$ and the right column represents the location $x = 4,000 \text{ m}$.

Because we composed the simulation domain with the assumption of flat ice shelf base and seabed, it is necessary to acquire high-resolution geometric data of the seabed and ice draft near the grounding line using autonomous underwater vehicles (Jenkins et al., 2010) to explore geometric effects. Specifically, investigating the structures and mechanisms of the buoyancy-driven circulation in the West Antarctic ice shelves is critical for understanding the rapid basal melting (Holland et al., 2020).

Our results and additional investigations on different types of ice shelves will aid in developing suitable parameters for correcting the heat flux or turbulent flux near the grounding line. Such a parameterization using the regional ocean model will reduce the uncertainty in the basal melting rate calculations. Moreover, examining

the ISW structures can be helpful in composing the various stability or shear conditions used in high-resolution studies (Gayen et al., 2016).

Data Availability Statement

The numerical model, PALM 6.0 (Rev:4552M) used in this study is available at (<https://palm.muk.uni-hannover.de/trac>). Initial and boundary conditions with numerical schemes can be set by the p3d file and the user interface codes are used to resolve the melting effect and ice shelf geometry. Detailed model configurations with melting effect parameterization are described in method section. HWD observation data in Figures 2a and 2b are referred from Davis and Nicholls (2019).

Acknowledgments

The authors are grateful to two anonymous reviewers for their helpful comments on the manuscript. This research was supported by Korea Institute of Marine Science & Technology Promotion (KIMST) funded by the Ministry of Oceans and Fisheries (RS-2023-00256677; PM23020) and Korea Polar Research Institute (KORPI) research grants (PE23440).

References

- Alley, K. E., Scambos, T. A., Siegfried, M. R., & Fricker, H. A. (2016). Impacts of warm water on Antarctic ice shelf stability through basal channel formation. *Nature Geoscience*, 9(4), 290–293. <https://doi.org/10.1038/ngeo2675>
- Arzeno, I. B., Beardley, R. C., Limeburner, R., Owens, B., Padman, L., Springer, S. R., et al. (2014). Ocean variability contributing to basal melt rate near the ice front of Ross Ice Shelf, Antarctica. *Journal of Geophysical Research: Oceans*, 119(7), 4214–4233. <https://doi.org/10.1002/2014JC009792>
- Begeman, C. B., Tulaczyk, S. M., Marsh, O. J., Mikucki, J. A., Stanton, T. P., Hodson, T. O., et al. (2018). Ocean stratification and low melt rates at the Ross Ice Shelf grounding zone. *Journal of Geophysical Research: Oceans*, 123(10), 7438–7452. <https://doi.org/10.1029/2018JC013987>
- Davis, P. E., & Nicholls, K. W. (2019). Turbulence observations beneath Larsen C ice shelf, Antarctica. *Journal of Geophysical Research: Oceans*, 124(8), 5529–5550. <https://doi.org/10.1029/2019JC015164>
- Dinniman, M. S., Asay-Davis, X. S., Galton-Fenzi, B. K., Holland, P. R., Jenkins, A., & Timmermann, R. (2016). Modeling ice shelf/ocean interaction in Antarctica: A review. *Oceanography*, 29(4), 144–153. <https://doi.org/10.5670/oceanog.2016.106>
- Gayen, B., Griffiths, R. W., & Kerr, R. C. (2016). Simulation of convection at a vertical ice face dissolving into saline water. *Journal of Fluid Mechanics*, 798, 284–298. <https://doi.org/10.1017/jfm.2016.315>
- Hellmer, H. H., & Olbers, D. J. (1989). A two-dimensional model for the thermohaline circulation under an ice shelf. *Antarctic Science*, 1(4), 325–336. <https://doi.org/10.1017/S0954102089000490>
- Hewitt, I. J. (2020). Subglacial plumes. *Annual Review of Fluid Mechanics*, 52(1), 145–169. <https://doi.org/10.1146/annurev-fluid-010719-060252>
- Holland, D. M., & Jenkins, A. (1999). Modeling thermodynamic ice–ocean interactions at the base of an ice shelf. *Journal of Physical Oceanography*, 29(8), 1787–1800. [https://doi.org/10.1175/1520-0485\(1999\)029<1787:MTIOIA>2.0.CO;2](https://doi.org/10.1175/1520-0485(1999)029<1787:MTIOIA>2.0.CO;2)
- Holland, D. M., Nicholls, K. W., & Basinski, A. (2020). The southern ocean and its interaction with the Antarctic ice sheet. *Science*, 367(6484), 1326–1330. <https://doi.org/10.1126/science.aaz5491>
- Holland, P. R. (2008). A model of tidally dominated ocean processes near ice shelf grounding lines. *Journal of Geophysical Research*, 113(C11), C11002. <https://doi.org/10.1029/2007JC004576>
- Jenkins, A. (1991). A one-dimensional model of ice shelf–ocean interaction. *Journal of Geophysical Research*, 96(C11), 20671–20677. <https://doi.org/10.1029/91JC01842>
- Jenkins, A. (1999). The impact of melting ice on ocean waters. *Journal of Physical Oceanography*, 29(9), 2370–2381. [https://doi.org/10.1175/1520-0485\(1999\)029<2370:TIOmio>2.0.CO;2](https://doi.org/10.1175/1520-0485(1999)029<2370:TIOmio>2.0.CO;2)
- Jenkins, A. (2016). A simple model of the ice shelf–ocean boundary layer and current. *Journal of Physical Oceanography*, 46(6), 1785–1803. <https://doi.org/10.1175/JPO-D-15-0194.1>
- Jenkins, A., Dutrieux, P., Jacobs, S. S., McPhail, S. D., Perrett, J. R., Webb, A. T., & White, D. (2010). Observations beneath Pine Island Glacier in West Antarctica and implications for its retreat. *Nature Geoscience*, 3(7), 468–472. <https://doi.org/10.1038/ngeo890>
- Kimura, S., Nicholls, K. W., & Venables, E. (2015). Estimation of ice shelf melt rate in the presence of a thermohaline staircase. *Journal of Physical Oceanography*, 45(1), 133–148. <https://doi.org/10.1175/JPO-D-14-0106.1>
- Li, Q., & Van Roekel, L. (2021). Towards multiscale modeling of ocean surface turbulent mixing using coupled MPAS–Ocean v6. 3 and PALM v5. 0. *Geoscientific Model Development*, 14(4), 2011–2028. <https://doi.org/10.5194/gmd-14-2011-2021>
- MacAyeal, D. R. (1984). Thermohaline circulation below the Ross Ice Shelf: A consequence of tidally induced vertical mixing and basal melting. *Journal of Geophysical Research*, 89(C1), 597–606. <https://doi.org/10.1029/JC089iC01p0597>
- Maronga, B., Gryscha, M., Heinze, R., Hoffmann, F., Kanani-Sühring, F., Keck, M., et al. (2015). The Parallelized Large-Eddy Simulation Model (PALM) version 4.0 for atmospheric and oceanic flows: Model formulation, recent developments, and future perspectives. *Geoscientific Model Development*, 8(8), 2515–2551. <https://doi.org/10.5194/gmd-8-2515-2015>
- McPhee, M. (2008). *Air-ice-ocean interaction: Turbulent ocean boundary layer exchange processes*. Springer Science & Business Media.
- Milillo, P., Rignot, E., Rizzoli, P., Scheuchl, B., Mougino, J., Bueso-Bello, J., & Prats-Iraola, P. (2019). Heterogeneous retreat and ice melt of Thwaites Glacier, West Antarctica. *Science Advances*, 5(1), eaau3433. <https://doi.org/10.1126/sciadv.aau3433>
- Morlighem, M., Rignot, E., Binder, T., Blankenship, D., Drews, R., Eagles, G., et al. (2020). Deep glacial troughs and stabilizing ridges unveiled beneath the margins of the Antarctic ice sheet. *Nature Geoscience*, 13(2), 132–137. <https://doi.org/10.1038/s41561-019-0510-8>
- Mueller, R. D., Padman, L., Dinniman, M. S., Erofeeva, S. Y., Fricker, H. A., & King, M. A. (2012). Impact of tide-topography interactions on basal melting of Larsen C Ice Shelf, Antarctica. *Journal of Geophysical Research*, 117(C5). <https://doi.org/10.1029/2011JC007263>
- Na, J. S., Kim, T., Jin, E. K., Yoon, S. T., Lee, W. S., Yun, S., & Lee, J. (2022). Large-eddy simulations of the ice-shelf–ocean boundary layer near the ice front of Nansen Ice Shelf, Antarctica. *The Cryosphere*, 16(9), 3451–3468. <https://doi.org/10.5194/16-3451-2022>
- Nakayama, Y., Cai, C., & Seroussi, H. (2021). Impact of subglacial freshwater discharge on Pine Island Ice Shelf. *Geophysical Research Letters*, 48(18), e2021GL093923. <https://doi.org/10.1029/2021GL093923>
- Nakayama, Y., Manucharyan, G., Zhang, H., Dutrieux, P., Torres, H. S., Klein, P., et al. (2019). Pathways of ocean heat towards Pine Island and Thwaites grounding lines. *Scientific Reports*, 9(1), 1–9. <https://doi.org/10.1038/s41598-019-53190-6>
- Nicholls, K. W., Makinson, K., & Venables, E. J. (2012). Ocean circulation beneath Larsen C Ice Shelf, Antarctica from in situ observations. *Geophysical Research Letters*, 39(19). <https://doi.org/10.1029/2012GL053187>

- Paolo, F. S., Fricker, H. A., & Padman, L. (2015). Volume loss from Antarctic ice shelves is accelerating. *Science*, *348*(6232), 327–331. <https://doi.org/10.1126/science.aaa0940>
- Pritchard, H., Ligtenberg, S. R., Fricker, H. A., Vaughan, D. G., van den Broeke, M. R., & Padman, L. (2012). Antarctic ice-sheet loss driven by basal melting of ice shelves. *Nature*, *484*(7395), 502–505. <https://doi.org/10.1038/nature10968>
- Raasch, S., & Schröter, M. (2001). P3. 13 a large-eddy simulation model performing on massively parallel computers.
- Ramudu, E., Gelderloos, R., Yang, D., Meneveau, C., & Gnanadesikan, A. (2018). Large eddy simulation of heat entrainment under Arctic sea ice. *Journal of Geophysical Research: Oceans*, *123*(1), 287–304. <https://doi.org/10.1002/2017JC013267>
- Rignot, E., Jacobs, S., Mouginot, J., & Scheuchl, B. (2013). Ice-shelf melting around Antarctica. *Science*, *341*(6143), 266–270. <https://doi.org/10.1126/science.1235798>
- Rignot, E., Mouginot, J., Scheuchl, B., Van Den Broeke, M., Van Wessem, M. J., & Morlighem, M. (2019). Four decades of Antarctic Ice Sheet mass balance from 1979–2017. *Proceedings of the National Academy of Sciences*, *116*(4), 1095–1103. <https://doi.org/10.1073/pnas.1812883116>
- Rosevear, M. G., Gayen, B., & Galton-Fenzi, B. K. (2022). Regimes and transitions in the basal melting of Antarctic ice shelves. *Journal of Physical Oceanography*, *52*(10), 2589–2608. <https://doi.org/10.1175/JPO-D-21-0317.1>
- Ruddick, B. (1983). A practical indicator of the stability of the water column to double-diffusive activity. *Deep-Sea Research*, *30*(10), 1105–1107. [https://doi.org/10.1016/0198-0149\(83\)90063-8](https://doi.org/10.1016/0198-0149(83)90063-8)
- Sharqawy, M. H., Lienhard, J. H., & Zubair, S. M. (2010). Thermophysical properties of seawater: A review of existing correlations and data. *Desalination and Water Treatment*, *16*(1–3), 354–380. <https://doi.org/10.5004/dwt.2010.1079>
- Stanton, T. P., Shaw, W. J., Truffer, M., Corr, H. F. J., Peters, L. E., Riverman, K. L., et al. (2013). Channelized ice melting in the ocean boundary layer beneath Pine Island Glacier, Antarctica. *Science*, *341*(6151), 1236–1239. <https://doi.org/10.1126/science.1239373>
- Timmermann, R., & Hellmer, H. H. (2013). Southern Ocean warming and increased ice shelf basal melting in the twenty-first and twenty-second centuries based on coupled ice-ocean finite-element modelling. *Ocean Dynamics*, *63*(9–10), 1011–1026. <https://doi.org/10.1007/s10236-013-0642-0>
- Vreugdenhil, C. A., & Taylor, J. R. (2019). Stratification effects in the turbulent boundary layer beneath a melting ice shelf: Insights from resolved large-eddy simulations. *Journal of Physical Oceanography*, *49*(7), 1905–1925. <https://doi.org/10.1175/JPO-D-18-0252.1>